South China Sea Wind Wave Characteristics

Part 1: Validation of Wavewatch-III Using TOPEX/POSEIDON Data

Peter C. Chu
Naval Ocean Analysis and Prediction Laboratory, Department of Oceanography
Naval Postgraduate School, Monterey, California

Yiquan Qi
South China Sea Institute of Oceanology
Chinese Academy of Sciences, Guangzhou, China

Yuchun Chen
Cold and Arid Regions Environmental and Engineering Research Institute
Lanzhou, China

Ping Shi, and Qingwen Mao
South China Sea Institute of Oceanology
Chinese Academy of Sciences, Guangzhou, China

Abstract

A full-spectral third-generation ocean wind-wave model, Wavewatch-III, has been implemented in the South China Sea (SCS) for investigating the wind wave characteristics. This model was developed at the Ocean Modeling Branch of the National Centers for Environmental Prediction (NCEP). The NASA QuickScat data (0.25^{o} resolution) two times daily were used to simulate the wind waves for the whole year in 2000. The significant wave heights from Wavewatch-III are compared to the TOPEX/POSEIDON (T/P) significant wave height data over the satellite crossover points in SCS. The model errors of significant wave height have Gaussian-type distribution with small mean value of 0.02 m (almost no bias). The model errors are comparable to the T/P altimeter accuracy (0.5 m) in the central SCS and smaller than the T/P altimeter accuracy in the northern and southern SCS, which indicates the capability of Wavewatch-III for SCS wave simulation.

1. Introduction

The South China Sea (SCS) is a semi-enclosed tropical sea located between the Asian land mass to the north and west, the Philippine Islands to the east, Borneo to the southeast, and Indonesia to the south (Fig. 1), a total area of 3.5 10^6 km^2. It connects to the East China Sea (through Taiwan Strait), the Pacific Ocean (through Luzon Strait), the Sulu Sea, the Java Sea (through Gasper and Karimata Straits), and to the Indian Ocean (through the Strait of Malacca). All of these straits are shallow except Luzon Strait whose maximum depth is 1800 m. The elliptical shaped central deep basin is 1900 km along its major axis (northeast-southwest) and approximately 1100 km along its minor axis, and extends to over 4000 m deep.

The SCS is under the influence of monsoon winds and synoptic systems such as fronts and tropical cyclones. From November to March, the northeasterly winter monsoon winds correspond to monthly mean January 2000 wind speeds of near 10 m/s for the whole SCS (Fig. 2a). From April to August, the southwesterly summer monsoon winds result in a monthly mean July 2000 wind speeds of approximate 8 m/s in the Southern SCS and 4 m/s in the northern SCS (Fig. 2b). The monthly mean winds (Fig. 2) are typical for monsoon winds. Highly variable winds and surface currents are observed during the transitional periods. Moreover, synoptic systems often pass by the SCS and causes temporally and spatially varying wind fields.

A fully spectral third-generation ocean wind-wave model, Wavewatch-III (henceforth denoted as WWATCH), has been recently developed at the Ocean Modeling Branch of the Environmental Modeling Center of the National Centers for Environmental

Prediction (NCEP) for the regional sea wave prediction. It was built on the base of Wavewatch-I and Wavewatch-II as developed at the Delft University of Technology, and NASA Goddard Space Flight Center, respectively (Tolman 1999).

WWATCH should be evaluated before the practical use. The highly variable wind systems and complicated topography make SCS a perfect location for WWATCH evaluation. Usually the in-situ wind wave data are mainly collected from voluntary ships and wave buoys. However, in SCS sparse voluntary ship data and no wave buoy data are available. The remote sensing is an important source for the wind wave data. Several satellites have been launched with altimetry, such as TOPEX/POSEIDON (T/P), ERS-1/2. The subsequent sections describe the WWATCH evaluation using the T/P significant wave height (SWH) data.

The outline of this paper is as follows: A description of data and WWATCH is given in Sections 2 and 3. Methodology and model evaluation are given in Sections 4 and 5. In Section 6, we present our conclusions.

2. Data

2.1. T/P SWH and Wind Speed

The T/P satellite, jointly launched by NASA and the French Space Agency, the Center National d'Etudes Spatiales (CNES) in August 1992, carried a state-of-the-art radar altimetry system (Fu et al. 1994). In addition to precise measurements of the distance between the satellite and the surface, SWH and wind speed are derived from the shape of the leading edge of the returning radar pulse. The accuracy of SWH measurement by T/P was within the accuracy of the Geosat measurements (Callahan et al. 1994), i.e., 10% or 0.5 m, whichever is greater (Dobson et al. 1987). T/P was

maneuvered into a 9.9156-day repeat period during which two T/P SWH and wind speed data are available at each crossover point. Time series of SWH at 20 crossover points (Fig. 3a) and at 4 passes (051, 229, 152, 190 in Fig. 3b) for 2000 are used to evaluate WWATCH.

2.2. QuikSCAT Sea Surface Winds

NASA launched the microwave scatterometer SeaWinds on the QuikBird satellite in June 1999. This instrument is referred to as QuikScat (or QSCAT). QSCAT is essentially a radar device that transmits radar pulses down to the Earth's surface and then measures the power that is scattered back to the instrument. This "backscattered" power is a measure of surface roughness. For water surfaces, the surface roughness is highly correlated with the near-surface wind speed and direction. Hence, wind speed and direction at a height of 10 meters over the ocean surface are retrieved from measurements of the QSCAT backscattered power. The backscattered power is also affected by rain.

The QSCAT Level 3 global surface wind data set consists of twice daily gridded values ($0.25^{o} \times 0.25^{o}$) of scalar wind speed, meridional and zonal components of wind velocity, wind speed squared and time given in fraction of a day. Presence of rain may degrade the accuracy of the QSCAT winds. Such degradation is indicated by rain probability determined using the Multidimensional Histogram (MUDH) Rain Flagging technique. Data are currently available in Hierarchical Data Format (HDF) and exist from 19 July 1999 to present.

3. WWATCH Model

3.1. Description

The wave spectrum F is generally a function of all phase parameters (i.e., wave number k, direction , intrinsic frequency σ, and absolute frequency ω), space ($\mathbf{x}$), and time (t),

$$F = F(k, \ , \sigma, \omega; \mathbf{x}, t).$$

However, the individual spectral components are usually assumed to satisfy the linear wave theory (locally) and to follow the dispersion relation,

$$\sigma^2 = gk \tanh kd \tag{1}$$

$$\omega = \sigma + \mathbf{k}\ \mathbf{U} \tag{2}$$

where d is the mean water depth and $\mathbf{U}$ is the (depth- and time- averaged) current velocity. When the current velocity vanishes, only two-phase parameters among (, k,) are independent. Current wave models use the frequency-direction (,) as the independent phase variables.

WWATCH uses the wavenumber-direction (k,) as the independent phase variables. Without currents, the energy of a wave package is conserved. With currents the energy of a spectral component is no longer conserved (Longuet-Higgins and Stewart 1961), but the wave action spectrum, $N(k,\theta; \mathbf{x}, t)$ $F(k,\theta; \mathbf{x}, t)/$, is conserved (Whitham 1965; Bretherthon and Garrett 1968). In WWATCH, the balance equation is for the wave action spectrum.

3.2. Model Setting

WWATCH has two types (mandatory and optional) of model switches for users to choose. Table 1 lists the model setting and optional switches for this study. For example,

spatial and spectral grids are user-defined; the ultimate quickest propagation scheme is selected with the dispersion correction from Booij and Holthuijsen (1987); nonlinear interactions are included; and the source term parameterization follows Tolman and Chalikov (1996) with consisting of four parts: wind input, nonlinear wave-wave interaction, dissipation, and wave-bottom interaction. The output of WWATCH consists of the traditional frequency-direction spectrum $F(\ ,\theta)$, which is calculated from $F(k, \theta)$ using Jacobean transformations.

3.3. Discretization

The model is implemented for SCS (0^o to 25^o N, 105°-122°E) using realistic bathymetry data from the Naval Oceanographic Office DBDB5 database and a regularly spaced longitude-latitude grid with the grid spacing 0.25^o (i.e., = $= 0.25^o$).

The wavenumber grid spacing is determined by the frequency intervals (total 25)

$$\sigma_{m+1} = X_\sigma \sigma_m, \ \text{m} = 0, 1, \ldots, 24, \tag{3}$$

with

$$X_\sigma = 1.1, \ \sigma_0 = 0.0418. \tag{4}$$

The wave direction ( ) grid spacing is 15^o (i.e., $= 15^o$).

Four time steps are used in WWATCH to reach computational efficiency: (a) global time step (300 s) for the propagation of the entire solution, (b) spatial time step (300 s) representing the spatial propagation, (c) spectral time step (300 s) for intra-spectral propagation, and (d) source time step (100 s) for the source term integration.

3.4. Wind Input and Friction Velocities

The surface winds (***W***) at each source time step (100 s) for the year of 2000 is interpolated from NASA SeaWinds on twice daily QuikScat (QSCAT) Level-3 gridded ocean wind vectors with 0.25° horizontal resolutions. The friction velocities are needed for the input source function S_{in}. In WWATCH, the friction velocity (u_*) is computed from the wind speed (W) at a given reference height z_r, in terms of a drag coefficient C_r (Tolman and Chalikov 1996)

$$u_*^2 = C_r W^2(z_r)\,. \tag{5}$$

An iteration process is adopted to obtain u_*. Wu's (1982) empirical relation

$$C_D(W) = 1.2875\times10^{-3} \qquad W < 7.5 \text{ m s}^{-1},$$

$$C_D(W) = (0.8 + 0.065W)\times10^{-3} \qquad W \geq 7.5\text{ms}^{-1}, \tag{6}$$

is used to obtain

$$u_*^{(0)} = \sqrt{C_D}\,W(z_{10})\,, \tag{7}$$

as the first guess friction velocity. Here, z_{10} = 10 m. The iteration stops when the change of the friction velocity is smaller than a prescribed criterion. Such iterations are performed during the model initialization, but are not necessary during the actual model run, as u_* changes slowly (Tolman 1999). The effect of the atmospheric instability on the friction velocity is parameterized using an effective wind speed W_e (Tolman and Booij 1998), which depends on the surface air and sea temperature difference.

3.5. Model Integration

WWATCH is integrated with twice daily gridded QSCAT ocean wind vectors (0.25°) from the JONSWAP 1973 wave spectra (Hasselmann et al. 1980) on January 3 (no sufficient wind data on January 1-2, 2000 for SCS), 2000 until 31 December 2000. The model SWH data are interpolated into the T/P crossover points. At each crossover

point, there are M pairs (approximately 72) of modeled (H_m) and observed (H_o) SWH data in 2000 (around 2 pairs per 10 days).

4. Methodology of Verification

4.1. Verification at Crossover Points

The difference of the modeled and observed SWH,

$$H = H_m(x, y, t) - H_o(x, y, t) \tag{8}$$

represents the model error. Bias, root-mean-square error (rmse), and correlation coefficient (cc) for each crossover point

$$\text{bias}(x, y) = \frac{1}{M}\sum_{i=1}^{M}\Delta H(x, y, t_i), \tag{9}$$

$$\text{rmse}(x, y) = \sqrt{\frac{1}{M}\sum_{i=1}^{M}\left[\Delta H(x, y, t_i)\right]^2}, \tag{10}$$

$$\text{cc}(x, y) = \frac{\sum_{i=1}^{M}\left[(H_m(x, y, t_i) - \bar{H}_m(x, y)\right]\left[(H_o(x, y, t_i) - \bar{H}_o(x, y)\right]}{\sqrt{\sum_{i=1}^{M}\left[(H_m(x, y, t_i) - \bar{H}_m(x, y)\right]^2}\sqrt{\sum_{i=1}^{M}\left[(H_o(x, y, t_i) - \bar{H}_o(x, y)\right]^2}}, \tag{11}$$

are used to verify WWATCH. Here $\bar{H}_m(x, y)$ and $\bar{H}_o(x, y)$ are temporal mean modeled and observed SWH,

$$\bar{H}_m(x, y) = \frac{1}{M}\sum_{i=1}^{M}H_m(x, y, t_i), \quad \bar{H}_o(x, y) = \frac{1}{M}\sum_{i=1}^{M}H_o(x, y, t_i), \tag{12}$$

at the crossover points. The T-value

$$T = \frac{\text{cc}\sqrt{\text{M-2}}}{\sqrt{1\text{-cc}^2}}, \tag{13}$$

with the degrees of freedom of (M - 2) is used for the significant test of cc.

4.2. Verification at Time Instance

Bias and rmse for time instance t

$$\text{bias}(t) = \frac{1}{N}\sum_{j,k} \Delta H(x_j, y_k, t)\,, \tag{14}$$

$$\text{rmse}(t) = \sqrt{\frac{1}{N}\sum_{j,k}\left[\Delta H(x_j, y_k, t)\right]^2}\,, \tag{15}$$

are also used to verify WWATCH.

5. Model Results

Two types of model-observation comparison are conducted: (1) horizontal SWH pattern using monthly mean data, and (2) model error statistics using synoptic crossover point SWH data (model and observation). To show the value-added of using WWATCH, the Pierson-Moskowitz (P-M) spectrum (1964) is also used for comparison in monthly mean horizontal SWH pattern.

5.1. Monthly Mean SWH

Three sets of monthly mean data are calculated from (a) modeled SWH using WWATCH, (b) calculated SWH using the P-M spectrum with the same QSCAT winds, and (c) observed SWH from T/P. A common feature in the simulated (Fig. 4), calculated (Fig. 5), and observed (Fig. 6) data shows that a higher SWHs in January (2000) than in July (2000).

In January (2000), a southwest to northeast oriented high SWH region (> 2.0 m) is comparable (north of 5° N) in the WWATCH simulation (Fig. 4a) and in the T/P data (Fig. 6a). However, this high SWH region is split into two smaller ones in the calculated (from P-M spectrum) field with a major one occurring north of 15°N and a minor one near the southern Vietnamese coast (Fig. 5a). The area with SWH larger than 2.5 m in the WWATCH simulation (113°–117°E, 15°–20°N) is comparable to that in the T/P data

(112°–117°E, 13°–20°N). Due to its independence on fetch, the P-M results show the SWH maximum of 3m near the northeast boundaries (upwind), which is not found in the simulated (WWATCH) and observed fields.

In July (2000), the mean SWHs are higher in the northern and central SCS (north of 10°N) than in the southern SCS (south of 10°N) with values larger than 2.25 m in the WWATCH simulated field (Fig. 4b) and than 2.5 m in the calculated (from P-M spectrum) (Fig. 5b) and observed fields (Fig. 6b). However, the maximum SWH values are located at (115°-120°E, 11°-15°N) in simulated and calculated fields and at (113°-116°E, 15°-20°N) in the observed field.

Due to its independence on fetch, the P-M results show the SWH maximum of 3m near the northeast boundaries (upwind) in January and of 2m near the southern boundaries in July (upwind), which is not found in the simulated (WWATCH) and observed fields. WWATCH simulates the seasonal variability of SWH reasonably well. SWH is larger in the winter than in the summer monsoon season. The orientation of the high SWH region coincides with the orientation of the monsoon winds (Fig. 2). The observed data show some more intensification in the maximum values. The SWHs show more irregular patterns using the P-M spectrum than using WWATCH. This is due to the coarse resolution in time the wind input (twice daily) that smoothes out extremes such as storm event (Chen et al. 2002).

5.2. Statistical Evaluation

The model-observation comparison is conducted at all 20 crossover points in SCS. Each one contains approximate 72 pairs of modeled (H_m) and observed (H_o) SWH data in 2000. The total number of pairs is 1330. The difference between the two, $H = H_m$

- H_o, is considered as the model error. The histogram of H [=H_m - H_o] (Fig. 7a) for all the 20 crossover points shows a Gaussian-type distribution with mean value (-0.02 m) and with comparable sample number of positive H (633) with negative H (697). The scatter diagrams for H_m and H_o show clustering of points approximately around the line of $H_m = H_o$ (Fig. 7b). The rmse and cc between H_m and H_o are 0.48 m and 0.90.

The scatter diagrams for H_m and H_o at each crossover points (Fig. 8) show spatial variability of the error statistics. The rmse increases from 0.34 m at southwest corner of SCS near Natuna Island [Point #1 (106.31^{o}E, 2.01^{o}N)] to 0.95 m in the central SCS near Zhongsha Island [Point #15 (114.81^{o}E, 17.18^{o}N)] and west of Luzon [Point #16 (117.65^{o}E, 17.20^{o}N)]. The bias varies from -0.45 m in the Gulf of Tonkin [Point #17 (107.73^{o}E, 20.59^{o}N)] to 0.33 m at the southern SCS near Nansha Island [Point #7 (114.81^{o}E, 9.8^{o}N)]. The correlation coefficient increases from 0.55 in the Gulf of Tonkin [Point #17 (107.73^{o}E, 20.59^{o}N)] to 0.95 in the central SCS near Zhongsha Island [Point #15 (114.81^{o}E, 17.18^{o}N)].

Contours of bias, rmse, and cc for the whole year (2000) are plotted (Fig. 9) to understand the spatial error variability. A positive bias occupies large portion of the SCS. The zero-bias contour follows 200-m bathymetry (Fig. 1) with negative bias on the continental shelf (west of the zero-bias contour) and positive bias in the deep basin (east of the zero-bias contour). A negative bias larger than –0.4 m is found in the Gulf of Tokin and a positive larger than 0.3 m is located near Nansha Island (115^{o}E, 10^{o}N) (Fig. 9a). This indicates that WWATCH-SCS overpredicts the SWH slightly except on the shallow continental shelf. The rmse of SWH is above 0.5 m in the central SCS with a maximum larger than 0.6 m west of Palawan (Fig. 9b). The value of rmse decreases from the central

SCS to the other two regions, and is smaller than 0.5 m in most of northern (west of Luzon) and southern (south of 5^{o}N) SCS.

Strong negative bias in the Gulf of Tonkin is obtained on the base of observations at a single crossover point (i.e., Point #17), which is quite close to the coast. The T/P altimeter data are not as valuable as in the deep sea. Recently, two high kinetic energy zones are identified as tidal fronts in the Qiongzhou Strait and near the southwestern coast of the Hainan Island (Hu et al. 2003). Tidal effect is not available in the model simulation.

The cc of SWH (Fig. 9c) between modeled and T/P data in 2000 is larger than 0.85 almost everywhere in SCS except in the Gulf of Tonkin. The T-value computed using (13) for cc = 0.85, M = 72 is: $T = 13.50$. For confidence coefficient $(1 - \alpha) = 0.095$, the t-distribution for the degree of freedom of statistics for (M - 2 = 70) is: $2.756 > t_{0.005} > 2.576$. Since T (= 13.50) is larger than $t_{0.005}$, the correlation coefficient between modeled and T/P SWH data is significant.

5.3. Spatial Error Variability along Three Ascending Tracks

Understanding the spatial error variability during different periods, four tracks (051, 229, 153, 190, see Fig. 3b) covering the SCS and three cycles (270, 288, and 302) are selected for the model evaluation. For each cycle, the T/P SWHs and wind speeds along the tracks are compared to the model simulated SWHs and QSCAT wind speeds (interpolated with the same temporal resolution with the T/P SWH and wind speed data).

5.3.1. Winter Monsoon Season (Cycle 270)

During Cycle 270, T/P passed over Track-051, -153, and -229 on January 14, 18, 19, and 21, respectively. The simulated and observed SWHs on the four tracks are

presented on the left panels in Fig. 10. The QSCAT and T/P wind speeds on the four tracks are presented on the right panels in Fig. 10.

Along Tracks-051, -229, and -190 (eastern and middle SCS) the simulated SWH coincides with T/P SWH quite well south of 12°N with errors usually less than 0.3 m and deviates from T/P SWH north of 12°N with errors larger than 1.0 m. Along Track-153 (western SCS) the simulated SWH is quite different from T/P SWH with errors larger than 1.0 m except for 10°–18°N segment.

After the gridded QSCAT winds are interpolated temporally at each source time step (100 s), the QSCAT and T/P wind speed pairs can be easily obtained along the T/P tracks with no spatial and temporal lags. QSCAT wind speeds agree with T/P wind speeds quite well along the tracks where the wind speed does not have strong spatial variability such as along Track-190. QSCAT wind speeds have large discrepancy along Track-153 south of 10°N and Trach-229 north of 20°N where the wind speed has strong spatial variability, with difference up to around 3-4 m s^{-1}. Comparison between left and right panels leads to a fact that discrepancy in SWH is correlated with wind speed error, except along Track-229, where the model errors do not well correlate to the wind errors. This may imply the importance of other source functions such as dissipation and nonlinear effect.

5.3.2. Summer Monsoon Season (Cycle 288)

During Cycle 288, T/P passed over Track-051, -153, 190, and -229 on July 10, 14, 16, and 17, respectively. The simulated and observed SWHs on the four tracks are presented on the left panels in Fig. 11. The QSCAT and T/P wind speeds on the four tracks are presented on the right panels in Fig. 11. Along Tracks-153 and -229 the

simulated SWH coincides with T/P SWH quite well with errors less than 0.5 m in most of latitudes. Along Tracks-051 and -190 the simulated SWH is quite different from T/P SWH with errors larger than 1.0 m in most latitudes.

QSCAT wind speeds agree with T/P wind speeds quite well along Track-153, which leads to a better SWH simulation along that track. QSCAT wind speeds have large discrepancy from the T/P wind speeds along Track-153, which leads to larger SWH errors along that track. Thus, the summer monsoon winds seem more difficult to resolve in the model. Quality of the wind input is important for SWH prediction.

5.3.3. Tropical Storm Rumbia 2000 (Cycles 302 and 303)

Cycles-302 and -303 during which Tropical Storm Rumbia 2000 was passing SCS with maximum guess strength of 25-30 m s^{-1} are selected for evaluation of model capability under strong and highly varying wind forcing. Tropical storm Rumbia initially formed about 800 km east of the Philippine island of Mindanao on 28 November 2000 (Fig. 12). After formation, Rumbia slowly intensified as it tracked westward through the Philippine Sea toward the central Philippine Islands. On 1 December, it made landfall over east Philippines and intensified to tropical storm strength, 18 m s^{-1} (measured by QSCAT). It continued moving westerly through the Philippine Islands, intensifying at a slow rate. After it enters the SCS, it continues to move westward and weakens and disappears on 9 December 2000 near the southern tip of Vietnam.

T/P passed over Track-190 (December 2) and Track-229 (December 3) during Cycle 302, and over Track-051 (December 6) and Track-153 (December 10) during Cycle 303. The simulated and observed SWHs (from T/P altimeter) on the three tracks are presented on the left panels in Fig. 13. The QSCAT and T/P wind speeds on the four tracks are

presented on the right panels in Fig. 13. Along Track-190 the simulated SWH coincides with T/P SWH quite well south of 17°N with mean error less than 0.5 m. Along Track-229 the simulated SWH is quite different from T/P SWH in central SCS (5°-18°N). QSCAT wind speeds agree with T/P wind speeds quite well along Track-190 south of 18°N, which leads to a better SWH simulation along that track. Wind speeds are quite different between QSCAT and T/P in central SCS (8°-18°N) along Track-229, which leads to larger SWH simulation errors along Track-229.

Poor performance during tropical storm Rumbia may be caused by too coarse grid resolution and lack of atmosphere-wave-ocean coupling. Chen et al. (2002) pointed out that simulation of typhoon or hurricane needs resolution from 1/6° for general structure to 2 km for detail eye-wall structure. With the extreme high winds, intense rainfall, large ocean waves, and copious sea spray the surface flux parameterization should be updated. This is illustrated by numerical simulation of air-sea interaction under high wind conditions using a coupled atmosphere-ocean-wave modeling system (Bao et al. 2000). Improvement of WWATCH for high wind conditions needs finer resolution and more realistic parameterization for surface momentum flux.

5.4. Temporal Error Variability at Selected Crossover Points

Understanding the temporal error variability, time series of H_m and H_o at four crossover points are presented (Fig. 14). WWATCH shows the capability in simulating SWH. Crossover point #2 (Fig. 14a) represents the southern SCS (Fig. 3). Bias, rmse, and cc at that point are 0.12 m, 0.41 m, and 0.92. The model errors do not have evident seasonal variability. That is to say that the model performance is equivalent during the prevailing monsoon seasons and during the monsoon transition periods.

Crossover point #6 represents the central SCS near 10°N (Fig. 3). Bias, rmse, and cc at that point are 0.03 m, 0.55 m, and 0.90. The model errors (Fig. 14b) are smaller during the (northeast) winter monsoon season (November - March) than during the (southwest) summer monsoon season (May - September).

Crossover point #11 represents the eastern part of central SCS (15°N) near Luzon Island (Fig. 3). Bias, rmse, and cc at that point are 0.09 m, 0.49 m, and 0.90. Different from crossover point #6, the model errors (Fig. 14c) are larger during the (northeast) winter monsoon season (November - March) than during the (southwest) summer monsoon season (May - September). For example, the SWHs are all well predicted during the summer monsoon season, however, during the winter monsoon period on February 2 the model simulated SWH (3.27 m) is much larger than the observed SWH (2.10 m).

Crossover point #19 represents the north SCS near 20°N (Fig. 3). Bias, rmse, and cc at that point are 0.07 m, 0.43 m, and 0.94. The model errors (Fig. 14d) are larger during the (northeast) winter monsoon season (November - March) than during the (southwest) summer monsoon season (May - September). For example, the SWHs are all well predicted during the summer monsoon season, however, during the winter monsoon period on December 7 the model simulated SWH (4.61 m) is much larger than the observed SWH (3.50 m).

5.5. **Temporal Error Variability for the Whole SCS**

The monthly mean bias and rmse averaged over all the crossover points in the SCS are presented in Fig. 15. They demonstrate the temporal error variability for the whole SCS. WWATCH-SCS has very low bias (-0.01 to 0.04 m) in predicting SWH with

a maximum (positive bias) value of 0.04 m in March and a minimum (negative bias) value of –0.01 m in April. The rmse has a minimum value of 0.39 m in March and a maximum value of 0.48 m in December.

6. Uncertainty in Surface Wind Data

Discrepancies between QSCAT and T/P wind speeds (right panels in Figs. 10-13) are found especially during the tropical storm Rumbia (2000) period (December 1-9, 2000), where the QSCAT winds are stronger than the T/P winds. Table 2 lists detail comparison between the two wind data sets. The root mean square difference between the two wind data sets increases from a minimum value of 1.12 m s^{-1} on January 14, 2000 (Cycle 270, Pass 051) to a maximum value of 3.70 m s^{-1} on December 3, 2000 (Cycle 302, Pass 229). The maximum difference between the two wind data sets increases from a minimum value of 2.87 ms^{-1} on January 14, 2000 (Cycle 270, Pass 051) to a maximum value of 11.92 m s^{-1} on December 3, 2000 (Cycle 302, Pass 229). Since the QSCAT winds are sensitive to rain, large discrepancy during the tropical storm Rumbia (2000) period may be caused by heavy rain.

7. Conclusions

Comparing the South China Sea significant wave height hindcast using the third generation wave model (Wavewatch-III) with significant wave height measured by TOPEX/POSEIDON altimeter for 2000, several characteristics of the model errors are obtained for the three subregions: central, northern, and southern SCS.

(1) Wavewatch-III simulates the seasonal variability of SWH reasonably well comparing to the T/P SWH data. July (2000) SWHs are higher in the northern and central

SCS (north of 10°N) than in the southern SCS (south of 10°N) with values up to 2.5 m in the WWATCH simulated field and 3.0 m in the observed fields. The orientation of the high SWH region coincides with the orientation of the monsoon winds.

(2) The model errors for SWH hindcast have Gaussian-type distribution with mean values of 0.02 m and with slightly more sample number on the negative side (697) than on the positive side (633). The root-mean-square error and correlation coefficient between modeled and observed significant wave heights are 0.48 m and 0.90.

(3) The model errors of WWATCH-SCS have spatial variability with overprediction of the SWH except on the shallow continental shelf. The rmse of SWH is above 0.5 m in the central SCS with a maximum larger than 0.6 m west of Palawan. The value of rmse northward and southward decreases from the central SCS, and is smaller than 0.5 m in most of northern (west of Luzon) and southern (south of 5°N) SCS.

(4) Over the whole SCS, WWATCH has very low bias (-0.01 to 0.04 m) in predicting SWH with a maximum (positive bias) value of 0.04 m in March and a minimum (negative bias) value of –0.01 m in April. The root-mean-square error has a minimum value of 0.39 m in March and a maximum value of 0.48 m in December.

(5) The model errors are comparable to the T/P altimeter accuracy (0.5 m) in the central SCS and smaller than the T/P altimeter accuracy in the northern and southern SCS, which indicates the capability of Wavewatch-III for SCS wave simulation.

(6) Ocean wave models are mainly forced by the surface winds. Difference between QSCAT and T/P wind speeds in this study indicates evident wind uncertainty. Modeling errors are caused by uncertain model external forcing (such as winds) or uncertain model internal structure (such as imperfect physics and resolution). Questions

arise: What is the contribution of external and internal uncertainty on modeling errors? How does error propagate from winds to ocean waves? Will the wind error be amplified or damped after it enters the ocean wave models? We will answer these questions in the second part of this paper.

Acknowledgements

The authors wish to thank Dr. Tolman at the National Weather Service for providing the Wavewatch-III model, the NOAA-CIRES Climate Diagnostics Center for providing NCEP Reanalysis data, and NASA/JPL for providing TOPEX/POSEIDON data. This work was jointly funded by the Naval Oceanographic Office, the Naval Postgraduate School, the Chinese Academy of Sciences (Project KZCX2-202), the National Natural Science Foundation of China (49976006), and the Science Foundation of Guangdong Province, China (990314).

References

Bao, J.-W., J.M. Wilczak, J.-K. Choi, and L.H. Kantha, 2000: Numerical simulation of air-sea interaction under high wind conditions using a coupled model: A study of hurricane development. Mon. Wea. Rev., 128 (7), 2190-2210.

Booij, N., and L.H. Holthuijsen, 1987: Propagation of ocean waves in discrete spectral wave models. J. Comput. Physics, 68, 307-326.

Bretherthon, F.P., and C.J.R. Garrett, 1968: Wave trains in inhomogeneous moving media. Proc. Roy. Soc. London, A 302, 529-554.

Callahan, P.S., C.S. Morris, and S.V. Hsiao, 1994: Comparison of TOPEX/POSEIDON $_0$ and significant wave height distributions to Geosat. J. Geophys. Res., 99, 25015-25024.

Chen, S.S., W. Zhao, J. E. Tenerelli, and M. Donelan, 2002: Atmosphere-wave-ocean coupling in tropical cyclones. 25th Conference on Hurricanes and Tropical Meteorology, Orlando, FL, April 28 - May 3, 2002.

Dobson, E., F. Monaldo, and J. Goldhirsh, 1987: Validation of Geosat altimeter-derived wind speeds and significant wave heights using buoy data, J. Geophys. Res., 92, 10719-10731.

Fu, L.L., E. J. Christensen, C.A. Yamaone Jr., M. Lefebvre, Y. Menard, M. Dorrer, and P. Escudier, 1994: TOPEX/POSEIDON mission overview. J. Geophys. Res., 99, 24369-24381.

Hasselmann, D.E., M. Dunckel, and J.A. Ewing, 1980: Directional wave spectra observed during JONSWAP 1973. J. Phys. Oceanogr., 10, 1264-1280.

Hu, J.-Y., H. Kawamura, and D.L. Tang, 2003: Tidal front around the Hainan Island, northwest of the South China Sea, J. Geophys. Res., 108, doi 10.1029/2003JC001883.

Longuet-Higgins, M. S., and R. W. Stewart, 1961: The changes in amplitude of short gravity waves on steady non-uniform currents. J. Fluid Mech., 10: 529-549.

Pierson, W.J., and L. Moskowitz, 1964: A proposed spectrum from a fully developed wind seas based on the similarity theory of S.A. Kitaigorodskii. J. Geophys. Res., 69, 5181-5190.

Tolman, H.L, 1999: User manual and system documentation of WAVEWATCH-III version 1.18, NOAA/NCEP Technical Note 166, pp. 110.

Tolman, H.L. and D.V. Chalikov, 1996: Source terms in a third-generation wind wave model. J. Phys. Oceaogr., 26:2497-2518.

Tolman, H.L. and N. Booij, 1998: Modeling wind waves using wavenumber-direction spectra and a variable wavenumber grid. Global atmosphere and ocean system. 295-309.

Whitham, G.B., 1965: A general approach to linear and non-linear dispersive waves using a Lagrangian. J. Fluid Mech., 22:273-283.

Wu, J., 1982: Wind stress coefficients over sea surface from breeze to hurricane. J. Geophys. Res., 87, 9704-9706.

Table 1 Model setting for this study.

Switch Parameters	Characteristics
DUM	Dummy to be used if WWATCH is to be installed on previously untried hardware
LRB8	8 byte words
SHRD	Shared memory model, no message passing
SEED	Seeding of high-frequency energy
GRD1	Settings directly hardwired to user-defined spatial grids (spherical coordinate with 0.25^{o} grids)
SP1	User-defined spectral grids.
PR2	Ultimate quickest propagation scheme with Booij and Holthuijsen (1987) dispersion correction
ST2	Tolman and Chalikov (1996) source term package
STAB2	Enable stability correction for Tolman and Chalikov (1996) source term package
NL1	Nonlinear interaction (DIA)
BT1	JONSWAP bottom friction formulation
WIND2	Approximately quadratic interpolation
CUR2	Approximately quadratic interpolation
o1	Output of boundary points in grid preprocessor
o2	Output of the grid point status map in grid preprocessor
o2a	Generation of land-sea mask file mask.ww3 in grid preprocessor
o3	Additional output in loop over fields in field preprocessor
o4	Print plot of normalized 1-D energy spectrum in initial conditions program
o5	2-D energy spectrum
o6	Spatial distribution of wave heights (not adapted for distributed memory)
o7	Echo input data for homogeneous fields in generic shell

Table 2 Root mean square difference and maximum difference between QSCAT and T/P wind speeds

Cycle Number	Pass Number	Number of Data-Pairs	Root mean square difference ($m\ s^{-1}$)	Maximum difference ($m\ s^{-1}$)
270	051	372	1.12	2.87
270	153	405	2.19	4.47
270	190	353	2.42	4.43
270	229	415	1.90	4.46
288	051	333	2.83	9.98
288	153	401	1.49	4.32
288	190	341	2.40	8.00
288	229	404	2.84	8.73
302	190	332	1.52	11.28
302	229	426	3.70	11.92
303	051	370	2.30	6.72
303	153	380	2.36	6.79

FIGURE CAPTIONS

Fig. 1. Geography and isobaths showing the bottom topography of the South China Sea.

Fig. 2. Monthly mean wind speed at 10 m height computed from the QSCAT data: (a) January 2000, and (b) July 2000.

Fig.3. T/P (a) crossover points and (b) tracks in the SCS.

Fig. 4. Simulated monthly mean SWH using WWATCH (a) January, and (b) July, 2000.

Fig. 5. Calculated monthly mean SWH using the Pierson-Moskowitz spectrum: (a) January, and (b) July, 2000.

Fig. 6. Monthly mean SWH from T/P data (a) January, and (b) July, 2000.

Fig 7. Model accuracy statistics: (a) histogram of model error, and (b) scatter diagram of modeled (H_m) and observed (H_o) SWH for all the crossover points.

Fig. 8. Scatter diagrams of SWHs at crossover points in the SCS.

Fig. 9. Distributions of SWH (a) bias, (b) rms error, and (c) correlation coefficient between WWATCH and T/P altimeter data for the whole year 2000.

Fig. 10. Comparison between modeled (dotted) and T/P observed (circle) SWHs (left panels) and QSCAT (dotted) and T/P observed wind speeds (circle) (right panels) along the four tracks during Cycle 270 (January 14-21, 2000).

Fig. 11. Comparison between modeled (dotted) and T/P observed (circle) SWHs (left panels) and QSCAT (dotted) and T/P observed wind speeds (circle) (right panels) along the four tracks during Cycle 288 (July 10-17, 2000).

Fig. 12. Track of tropical storm Rumbia 2000**.**

Fig. 13. Comparison between modeled (dotted) and T/P observed (circle) SWHs (left panels) and QSCAT (dotted) and T/P observed wind speeds (circle) (right panels) along the four tracks during Cycle 302, 303 (December 03-09, 2000), when Tropical Storm RUMBIA passed over the SCS.

Fig. 14. Comparison between WWATCH modeled (solid curve) and T/P observed (denoted by circle) significant wave heights at (a) Point #2, (b) Point #6, (c) Point #11, and (d) Point #19.

Fig. 15. Temporal evolution of (a) bias and (b) rmse for the whole SCS.

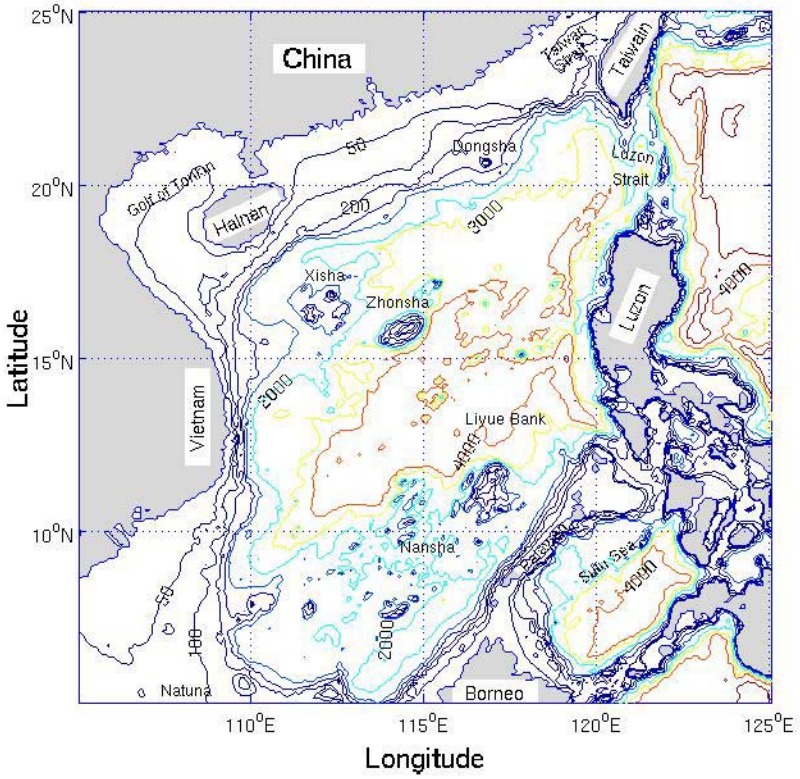

Fig. 1. Geography and isobaths showing the bottom topography of the South China Sea.

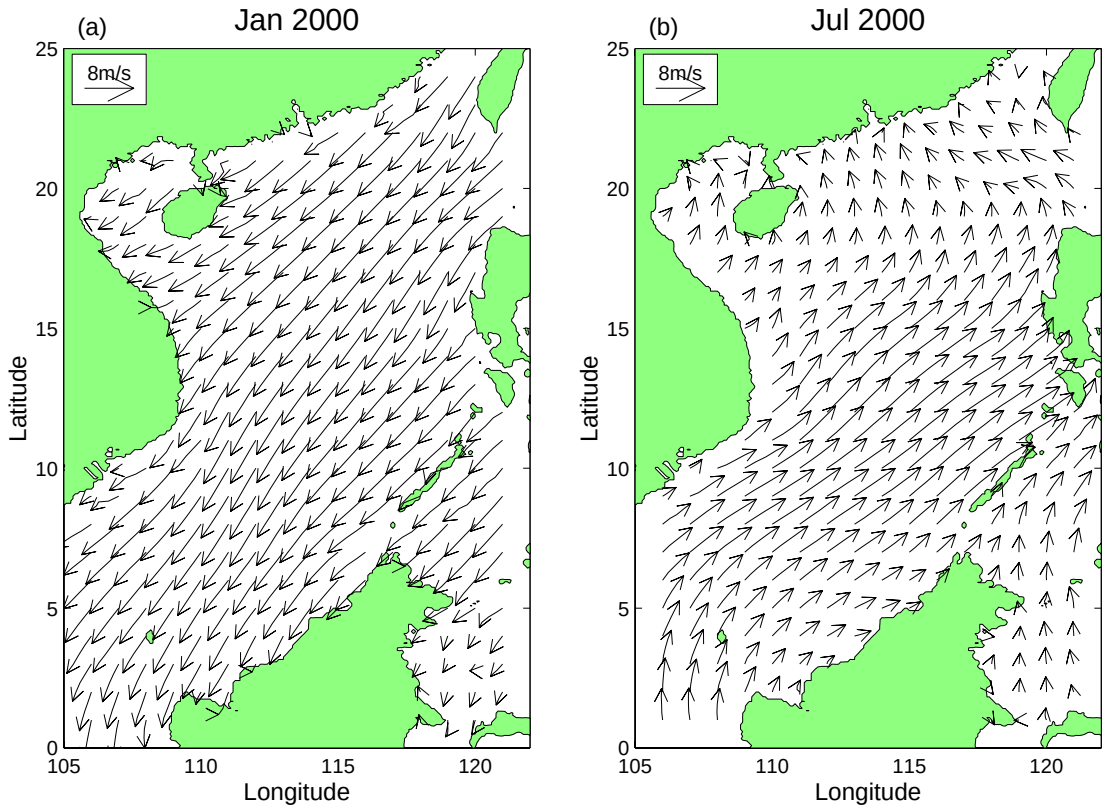

Fig. 2. Monthly mean wind speed at 10 m height computed from the Quikscat data: (a) January 2000, and (b) July 2000.

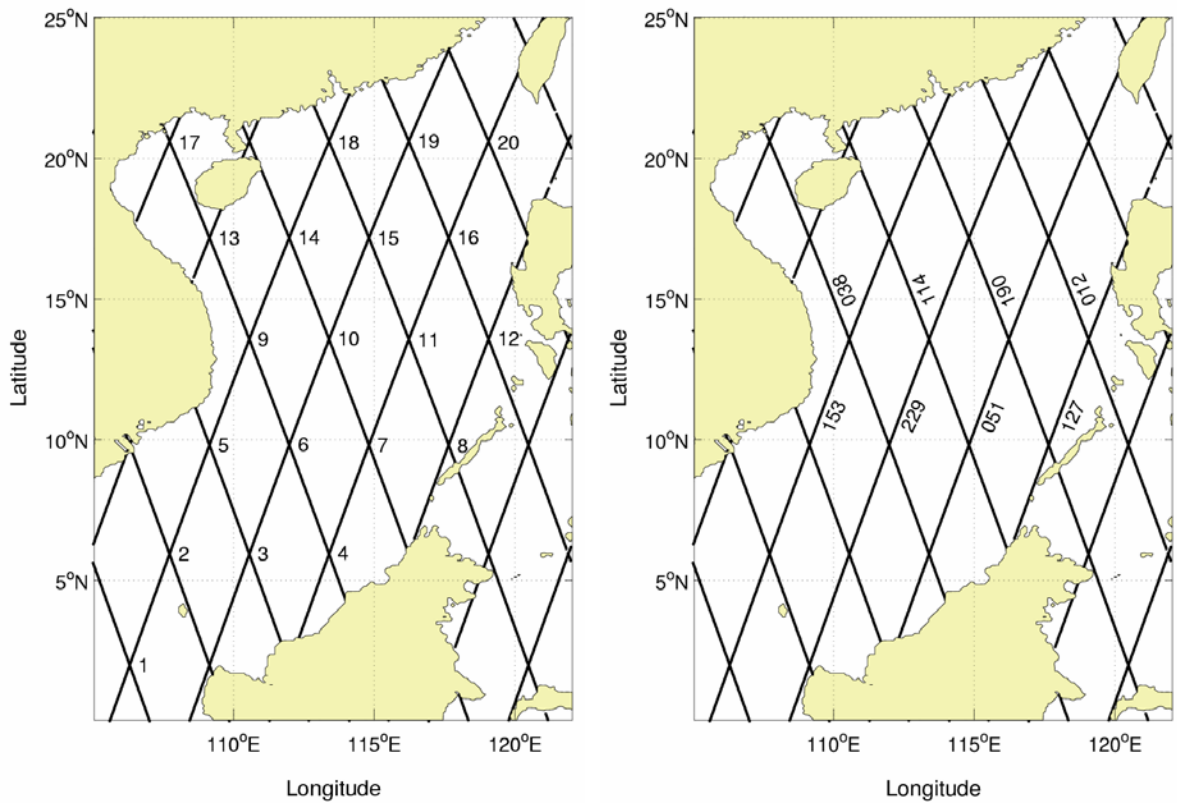

Fig.3. T/P (a) crossover points and (b) tracks in the SCS.

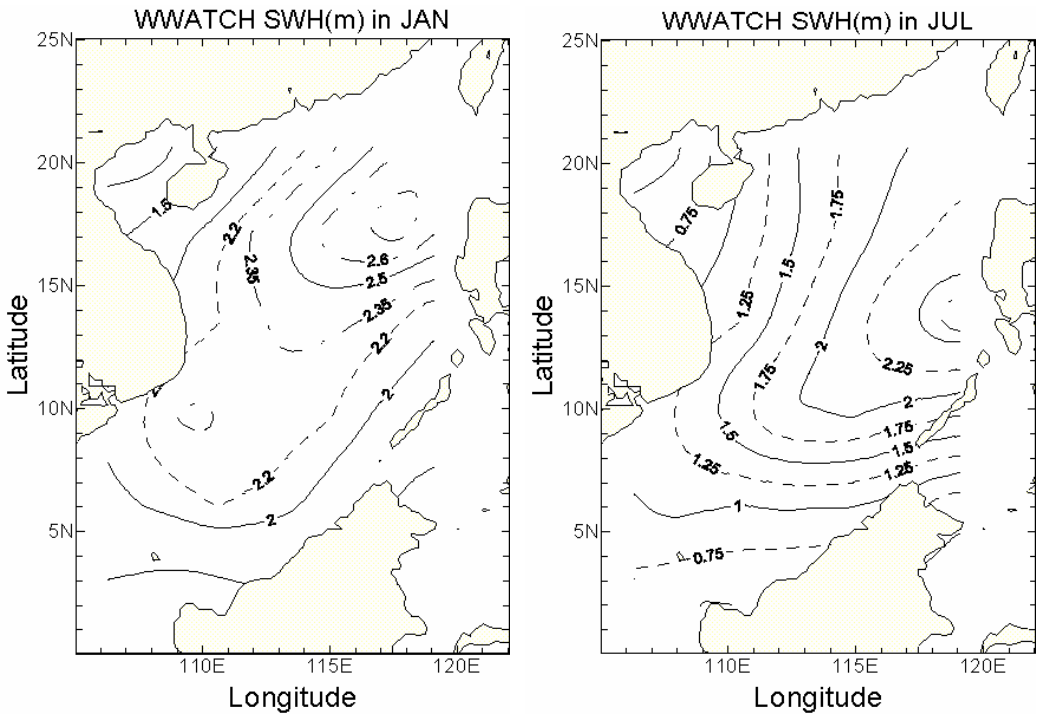

Fig. 4. Predicted monthly mean SWH using WWATCH (a) January, and (b) July, 2000.

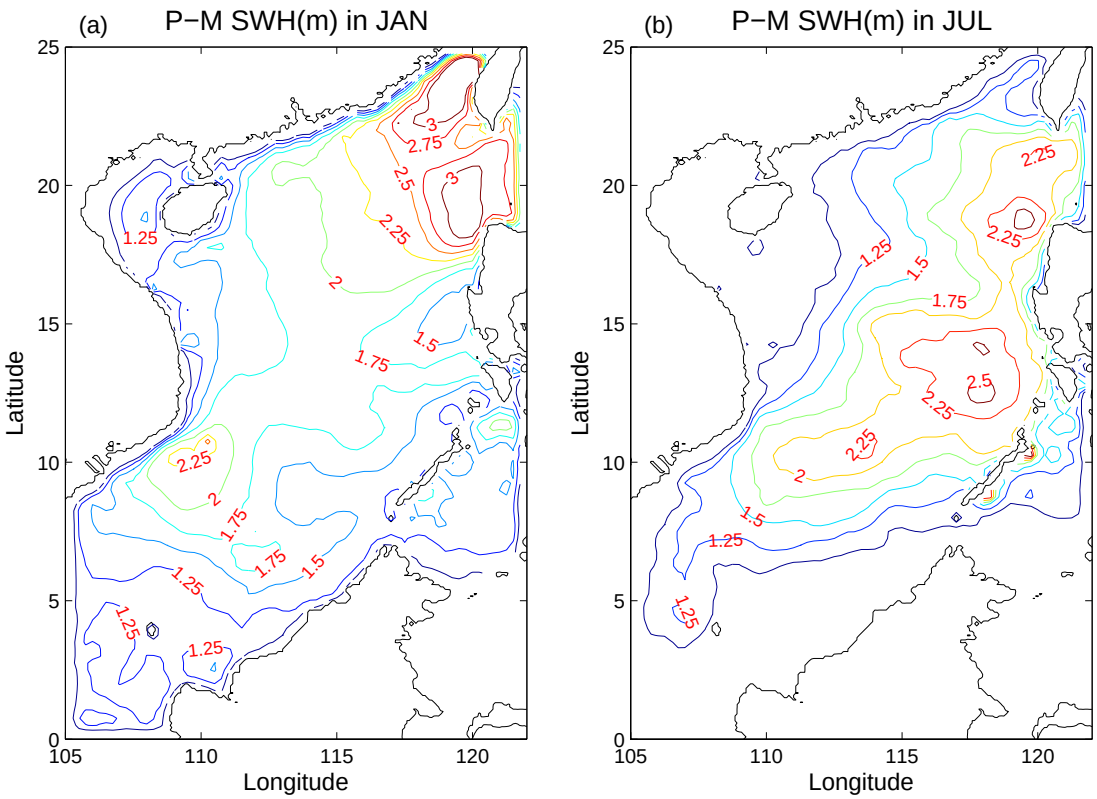

Fig. 5. Calculated monthly mean SWH using the Pierson-Moskowitz spectrum: (a) January, and (b) July, 2000.

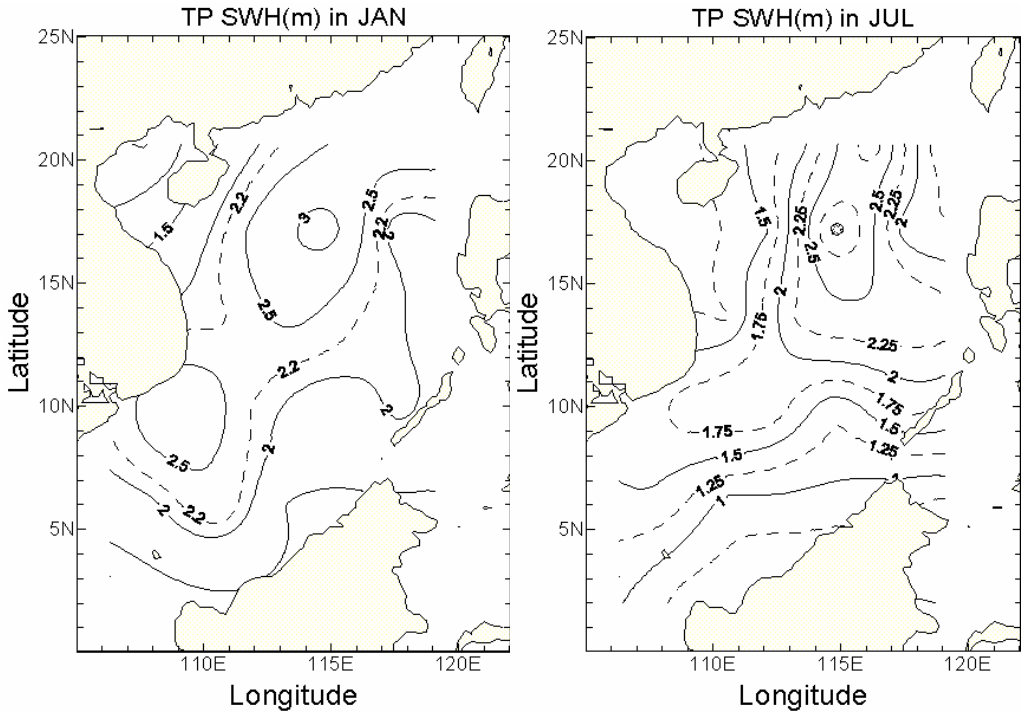

Fig. 6. Monthly mean SWH from T/P data (a) January, and (b) July, 2000.

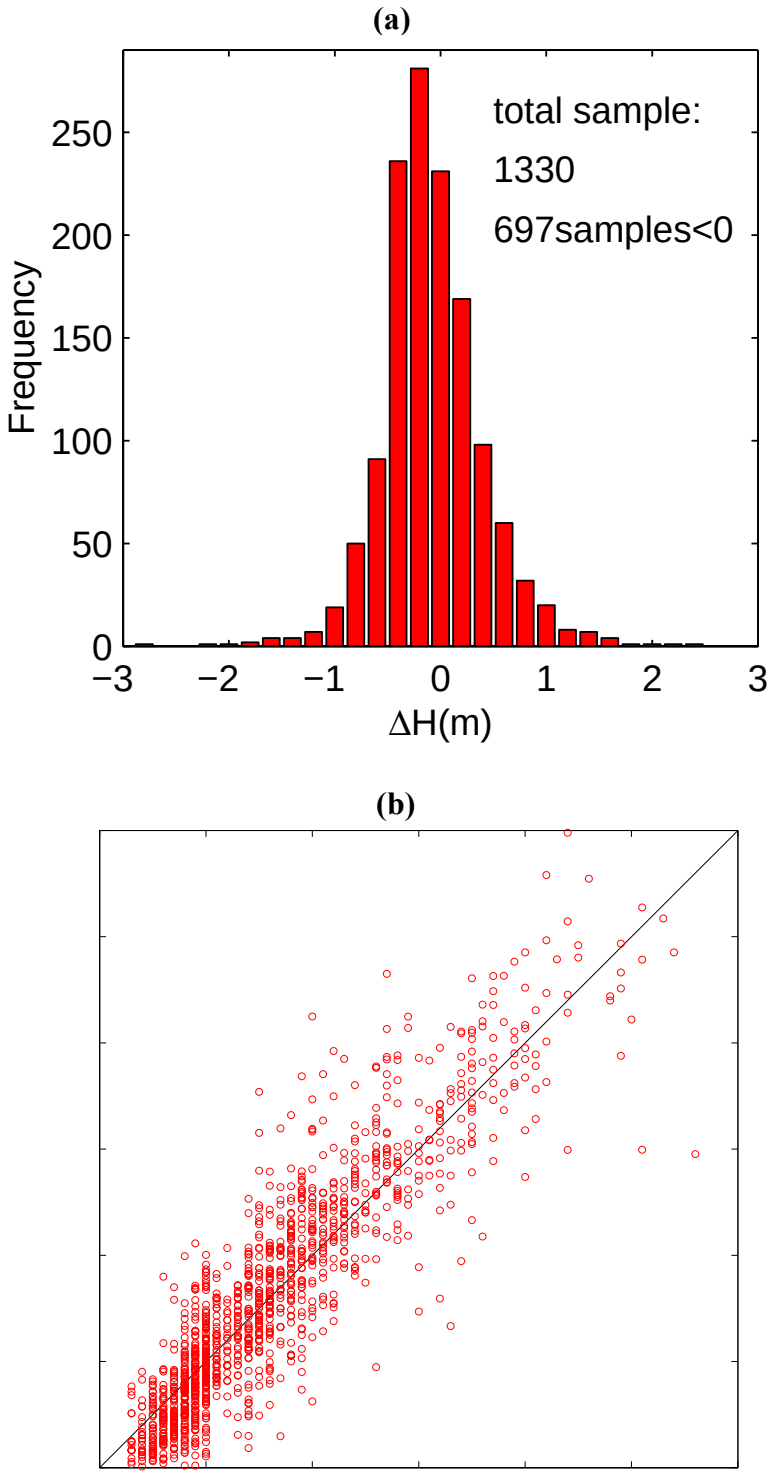

Fig. 7. Model accuracy statistics: (a) histogram of model error, and (b) scatter diagrams of modeled (H_m) and observed (H_o) SWH for all the crossover points.

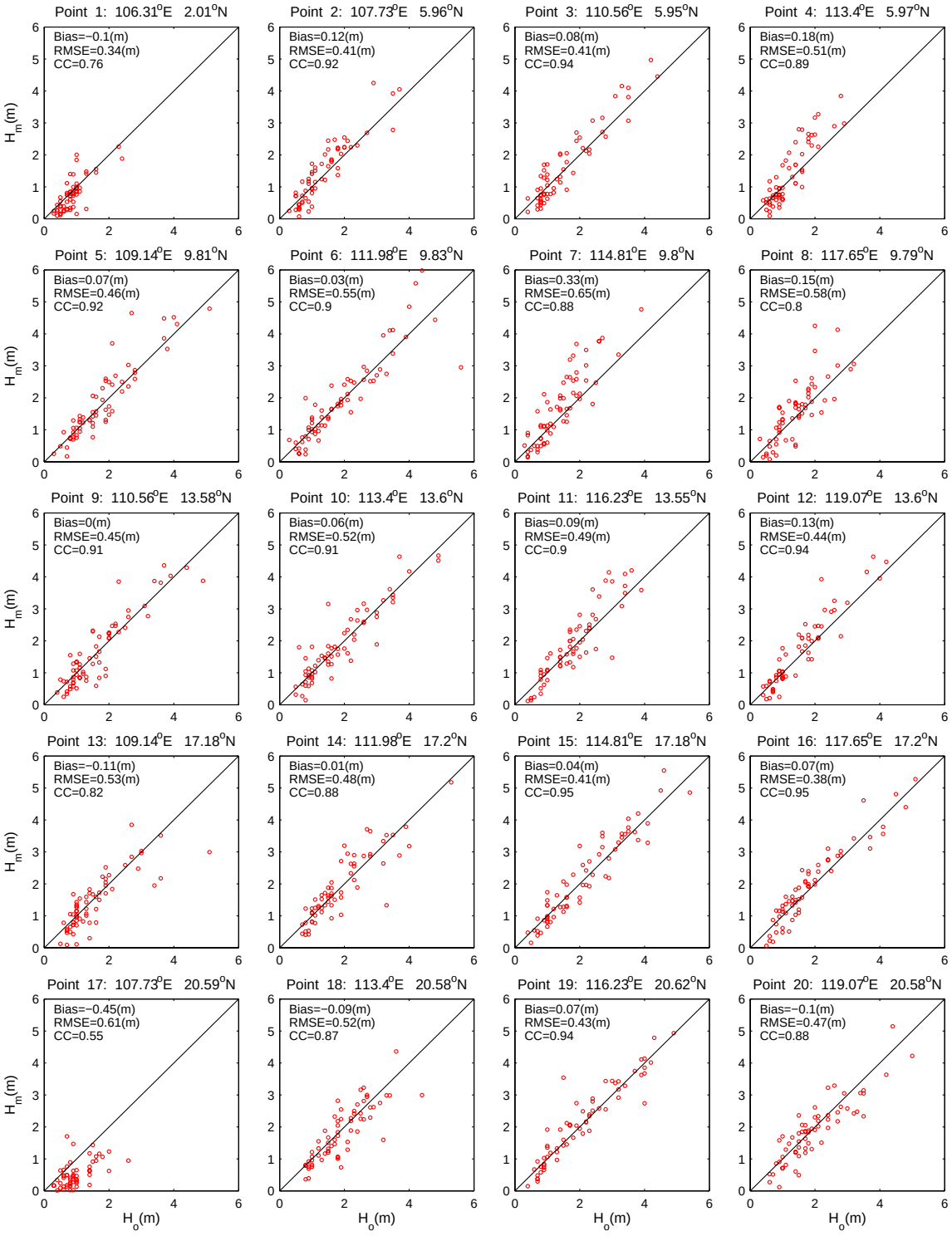

Fig. 8. Scatter diagrams of SWHs at crossover points in SCS.

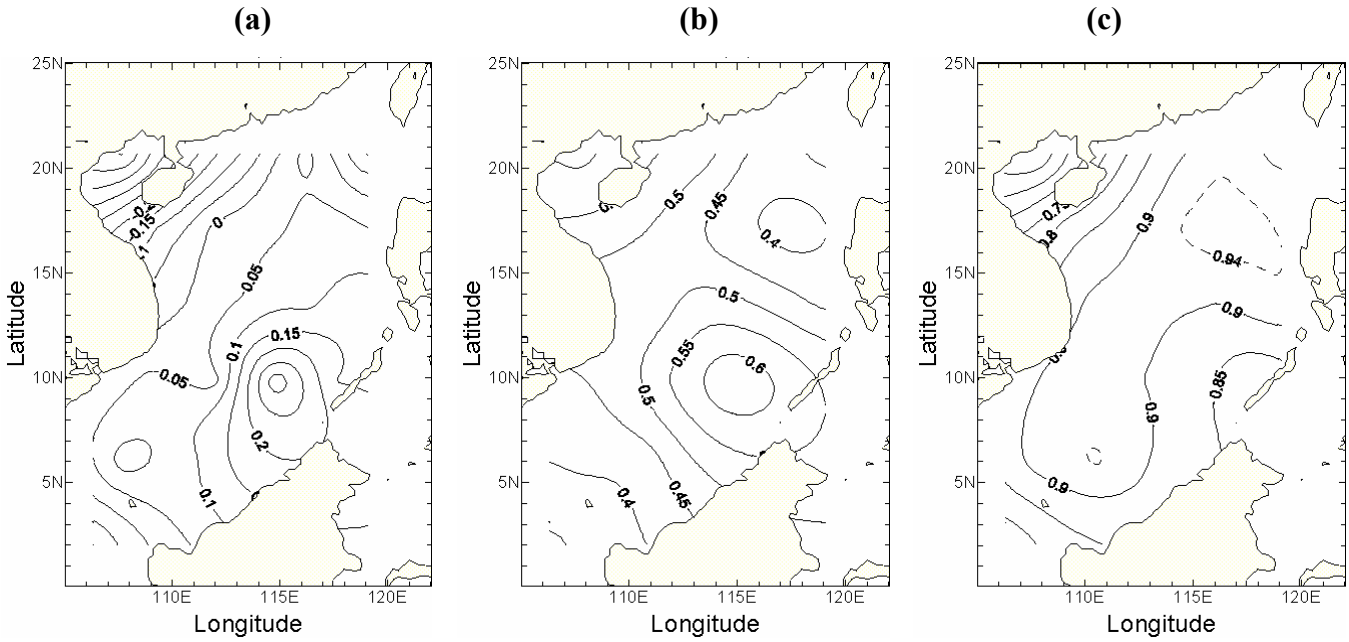

Fig. 9. Distributions of SWH (a) bias, (b) rms error, and (c) correlation coefficient between WWATCH and T/P data.

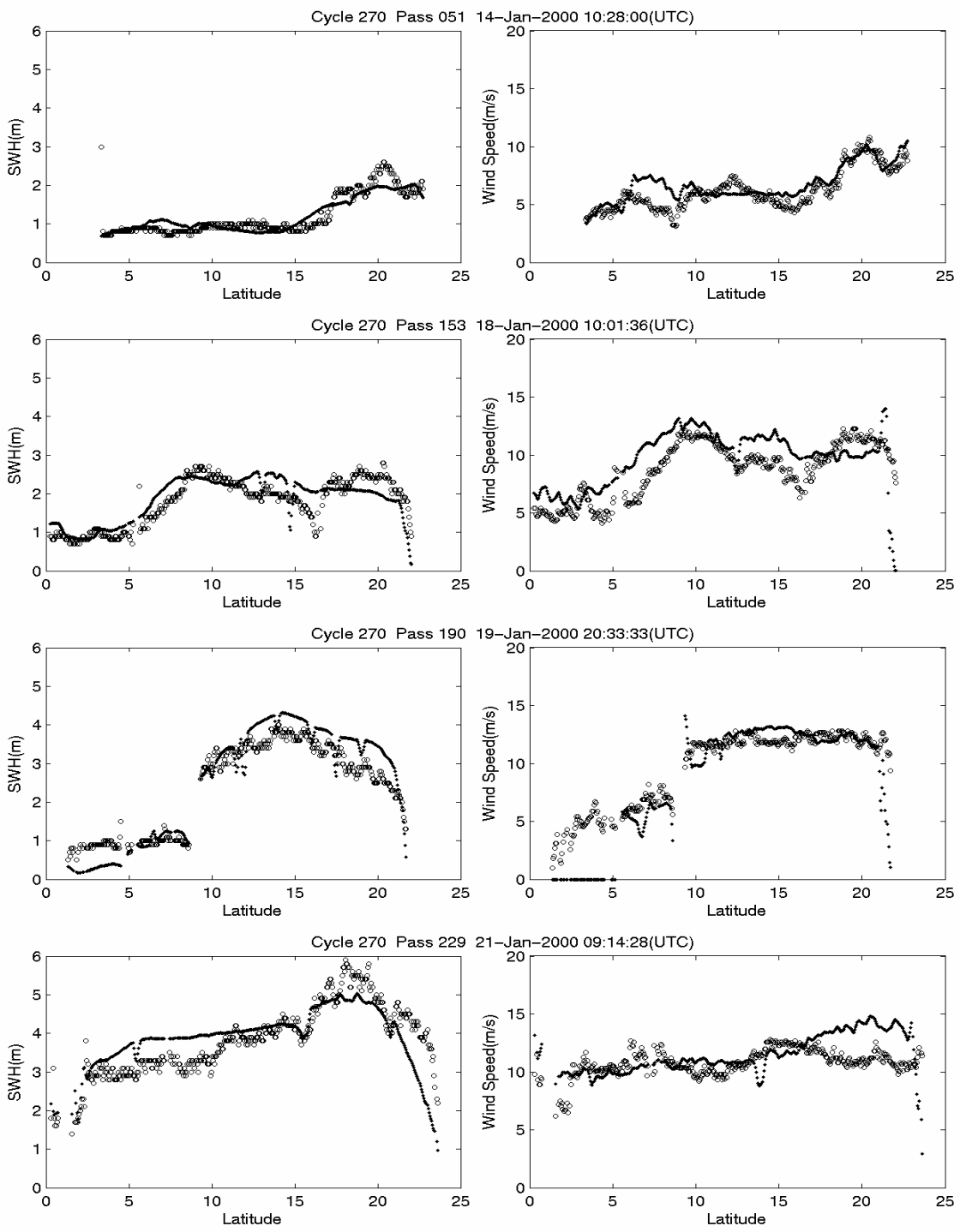

Fig. 10. Comparison between modeled (solid) and T/P observed (dotted) SWHs (left panels) and QuikSCAT (solid) and T/P observed wind speeds (dotted) (right panels) along the four tracks during Cycle 270 (January 14-21, 2000).

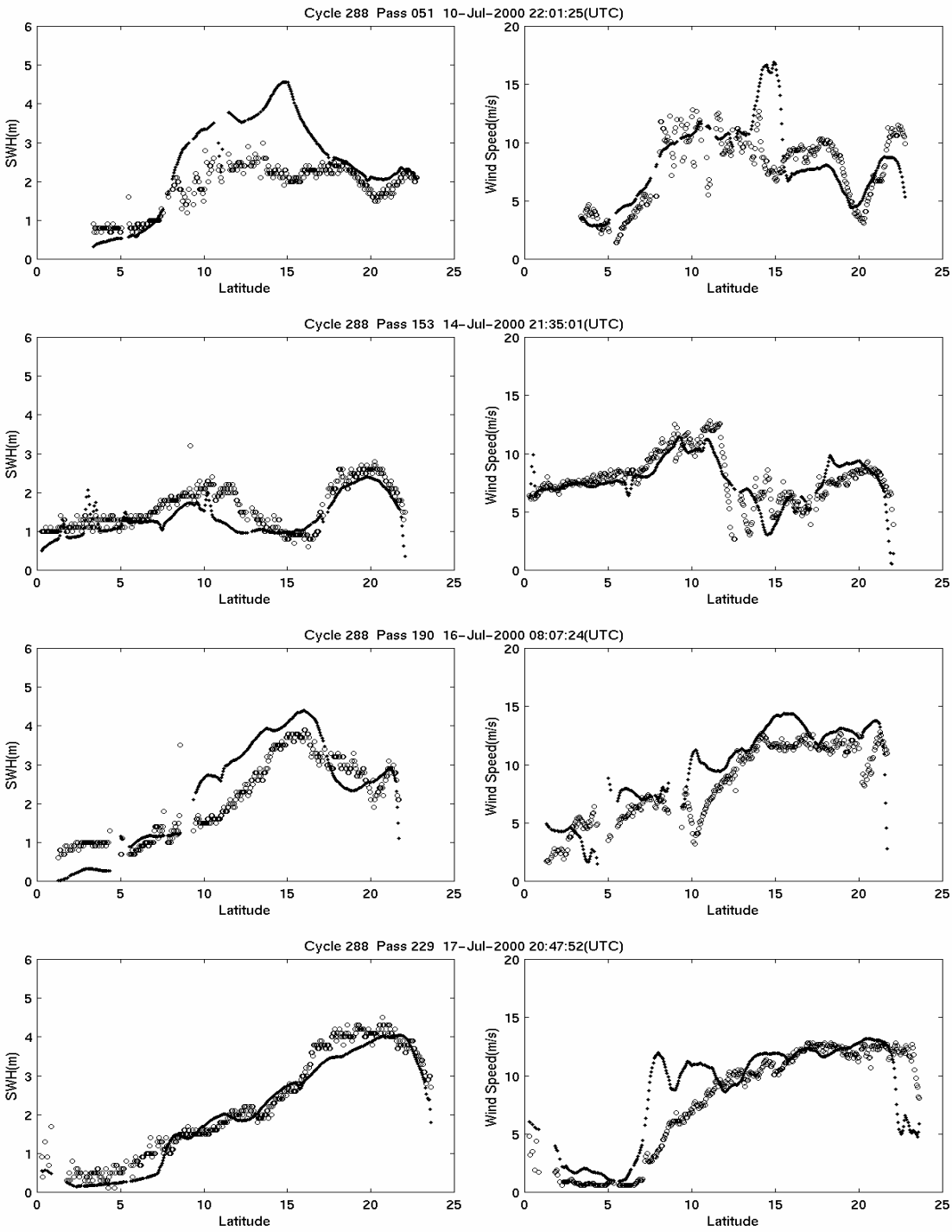

Fig. 11. Comparison between modeled (solid) and T/P observed (dotted) SWHs (left panels) and QuikSCAT (solid) and T/P observed wind speeds (dotted) (right panels) along the four tracks during Cycle 288 (July 10-17, 2000).

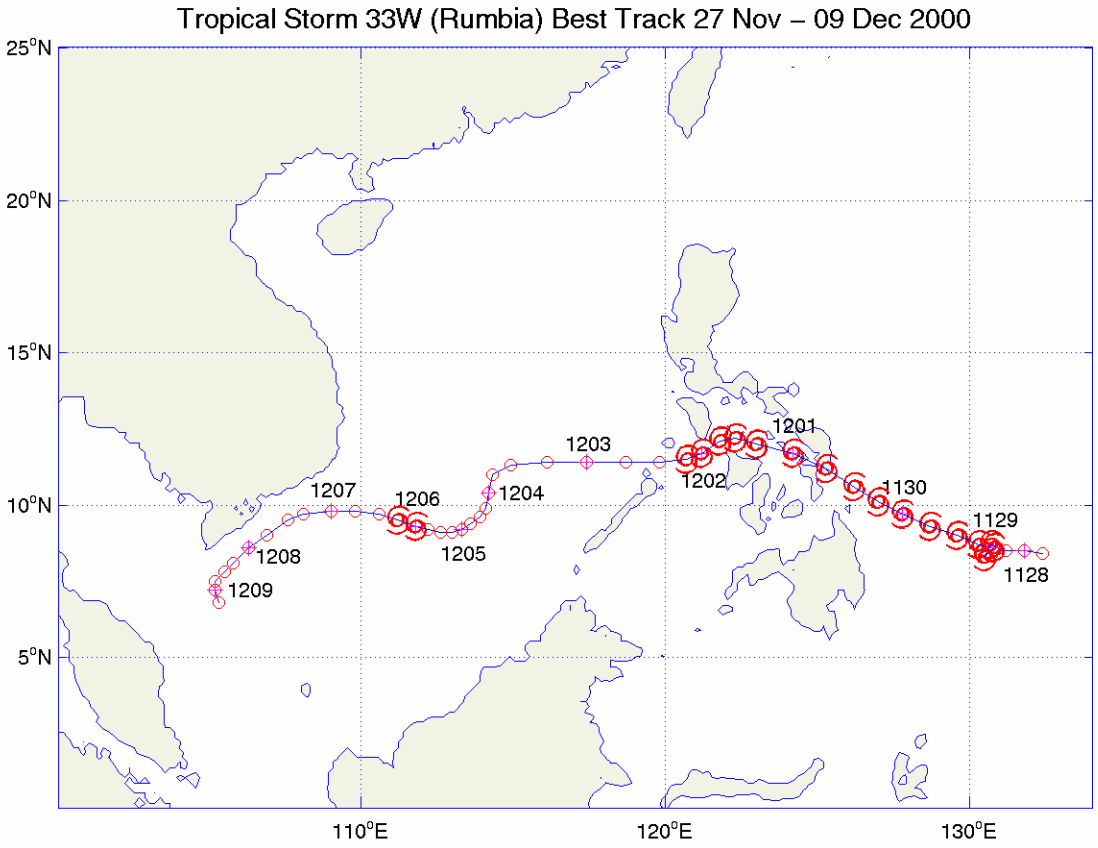

Fig. 12. Track of tropical cyclone Rumbia 2000.

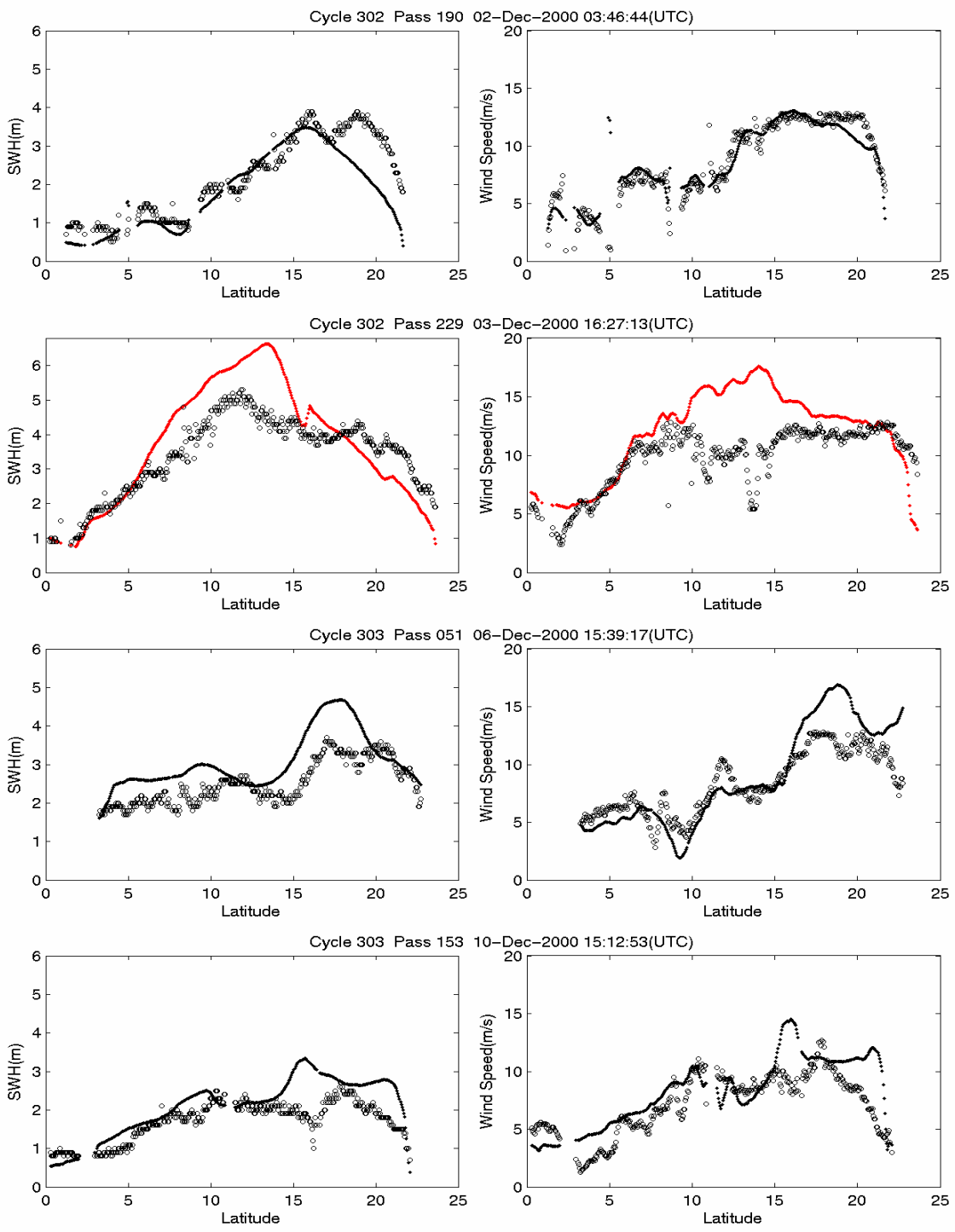

Fig. 13. Comparison between modeled (solid) and T/P observed (dotted) SWHs (left panels) and QuikSCAT (solid) and T/P observed wind speeds (dotted) (right panels) along the four tracks during Cycle 302,303 (December 03-09,2000), When Tropical Cyclone RUMBIA passed over the SCS.

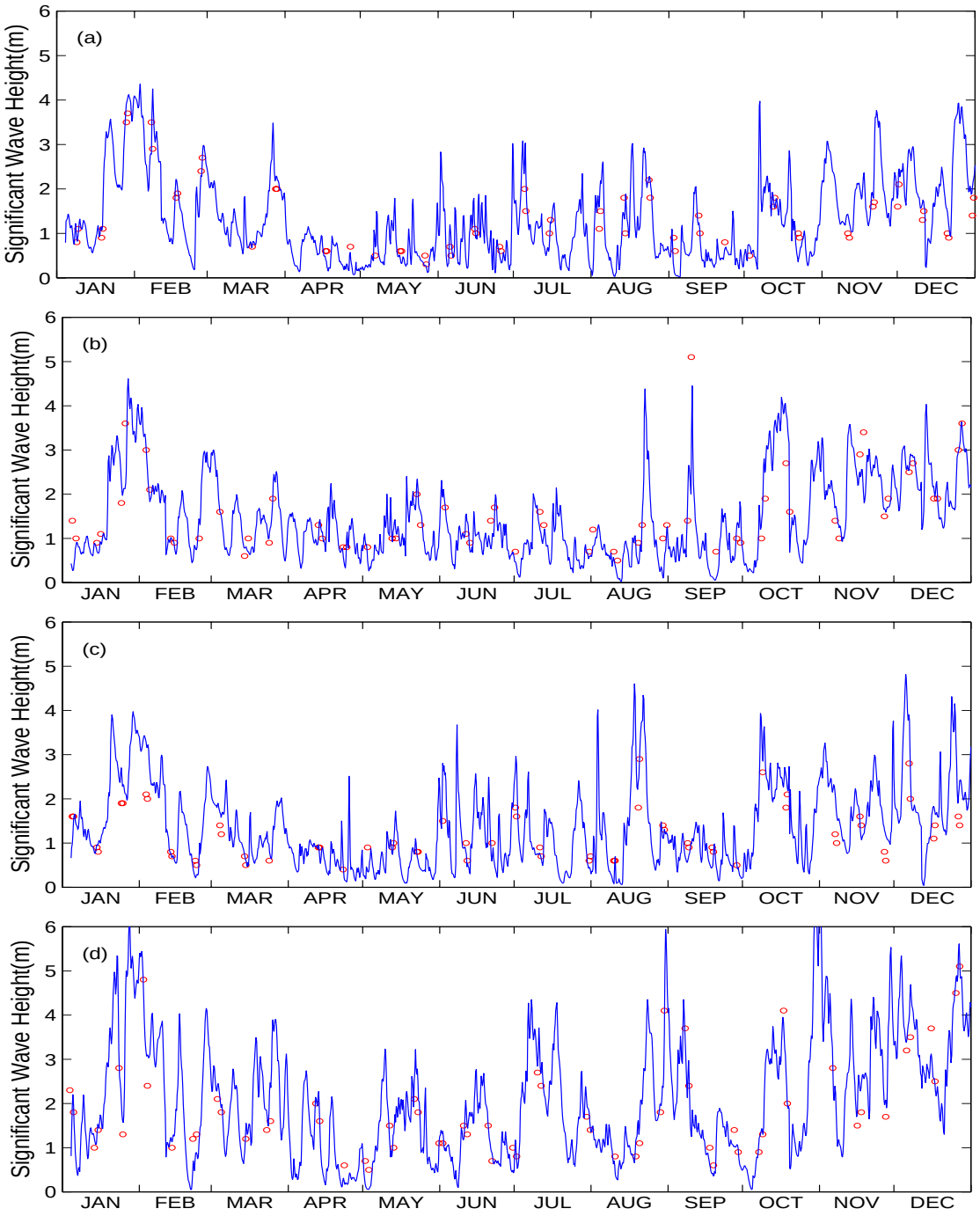

Fig. 14. Comparison between WWATCH modeled (solid curve) and T/P observed (denoted by circle) significant wave heights at (a) Point #2, (b) Point #6, (c) Point #11, and (d) Point #19.

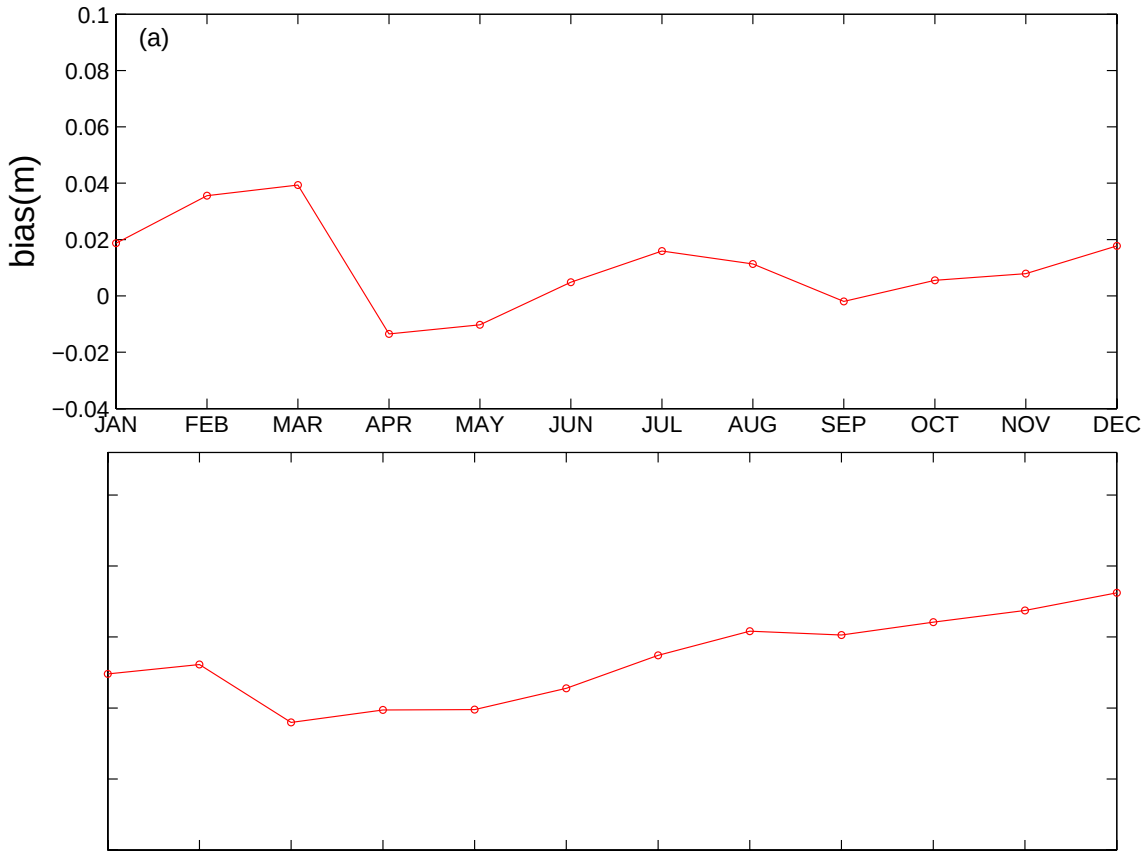

Fig. 15. Temporal evolution of (a) bias and (b) rmse for the whole SCS.